Available online at www.sciencedirect.com

ScienceDirect

journal homepage: www.elsevier.com/locate/he

H_2-rich syngas production from biogas reforming: Overcoming coking and sintering using bimetallic Ni-based catalysts

S. Carrasco-Ruiz [a], Q. Zhang [b], J. Gándara-Loe [a], L. Pastor-Pérez [a], J.A. Odriozola [a,b], T.R. Reina [a,b,**], L.F. Bobadilla [a,*]

[a] Inorganic Chemistry Department and Materials Science Institute, University of Seville-CSIC, 41092, Sevilla, Spain
[b] Department of Chemical and Process Engineering, University of Surrey, Guildford, GU2 7XH, UK

HIGHLIGHTS

- H_2-rich syngas can be obtained efficiently from biogas reforming.
- Ni-based catalysts are deactivated by metal sintering and coke deposition.
- Doping with low Rh loadings deactivation can be successfully prevented.

GRAPHICAL ABSTRACT

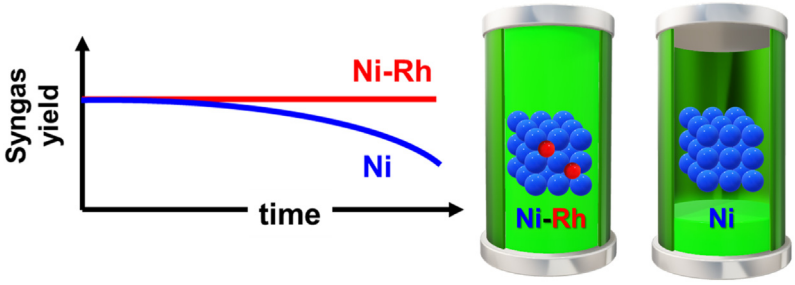

ARTICLE INFO

Article history:
Received 23 August 2022
Received in revised form
11 February 2023
Accepted 20 March 2023
Available online 19 April 2023

Keywords:
Dry reforming
H_2-rich syngas
Ni–Rh catalyst
Coking resistance

ABSTRACT

Dry reforming of methane is a very appealing catalytic route biogas (mainly composed by greenhouse gases: carbon dioxide and methane) conversion into added value syngas, which could be further upgraded to produce liquid fuels and added value chemicals. However, the major culprits of this reaction are coking and active phase sintering that result in catalysts deactivation. Herein we have developed a highly stable bimetallic Ni–Rh catalyst supported on mixed CeO_2–Al_2O_3 oxide using low-noble metal loadings. The addition of small amounts of rhodium to nickel catalysts prevents coke formation and improves sintering resistance, achieving high conversions over extended reaction times hence resulting in promising catalysts for biogas upgrading.

* *Corresponding author.*
** *Corresponding author.* Inorganic Chemistry Department and Materials Science Institute, University of Seville-CSIC, 41092, Sevilla, Spain.
E-mail addresses: t.ramirezreina@surrey.ac.uk (T.R. Reina), lbobadilla@us.es (L.F. Bobadilla).

https://doi.org/10.1016/j.ijhydene.2023.03.301

Introduction

Fighting global warming alert to mitigate the negative human impact on the environment is one of the urgent priorities of the scientific community raking top as Global Challenge priority for a sustainable development. The greenhouse effect caused by the emission of harmful gases into the atmosphere is provoking an increase in global temperature and therefore to changing climates causing droughts, deforestation, and desertification of the planet.

The four main greenhouse gases (GHG) attracting serious global attention today are CO_2, CH_4, SO_2, and N_2O. Carbon dioxide is by far the most emitted gas into the atmosphere, accounting for 76% of total emissions in 2019 [1]. According to *United in Science 2020* [2], a report compiled by the World Meteorological Organization (WMO) under the direction of the United Nations Secretary-General, lockdown-related fall in emissions caused by COVID-19 pandemic will not reduce sufficiently the CO_2 concentrations in the atmosphere. The growing trend of CO_2 and CH_4 emissions driven by the increase of global energy consumption makes mandatory the search of alternatives to achieve GHG valorisation [3].

The use of renewable energy sources represents "must do" action to favour the transition towards a low-carbon economy. Herein, biogas can play an important role in the development of the renewable energy market nowadays, as it has a wide variety of applications compared to other renewable energy sources [4]. Biogas is produced by anaerobic digestion of biodegradable wastes and is mainly compound by carbon dioxide and methane [5,6]. After its production, there are three main routes for biogas utilisation (Fig. 1b).

- Biomethane is a nearly pure methane stream that can be obtained by CO_2 separation of biogas. At present, biomethane has been widely used as an engine vehicle fuel in many countries and has broad development prospects [7,8].
- Biogas is a raw material to produce syngas (H_2/CO gas mixture) for industrial syntheses or energy purposes [7]. There are several ways to reform biogas into syngas such as Dry Reforming of Methane or Bi-Reforming of Methane.
- Green electricity can be produced from biogas by Combined Heat & Power system (CHP) [9].

Syngas is a combustible gas that can be used to produce electrical energy in turbines and fuel cells (Fig. 1c), but the current market demand uncovers the potential of syngas as a feedstock to produce fuels like diesel, naphtha, and gasoline, as well as for high value-added chemical inputs via Fischer-Tropsch synthesis (FTS) [10].

Focusing on biogas upgrading, there several thermal catalytic routes for syngas production from biogas namely: Oxy-Reforming of Methane (ORM), Bi-Reforming of Methane (BRM) and Dry Reforming of Methane (DRM) [11]:

$$ORM: 3\,CH_4 + CO_2 + O_2 \rightleftharpoons 4\,CO + 6\,H_2 \quad \text{(Eq.1)}$$

$$\Delta H^0 = 58\ kJ/mol$$

$$\Delta G^0 = -1\ kJ/mol$$

$$BRM: 3\,CH_4 + CO_2 + 2\,H_2O \rightleftharpoons 4\,CO + 8\,H_2 \quad \text{(Eq.2)}$$

$$\Delta H^0 = 220\ kJ/mol$$

$$\Delta G^0 = 151\ kJ/mol$$

$$DRM: CH_4 + CO_2 \rightleftharpoons 2\,CO + 2\,H_2 \quad \text{(Eq.3)}$$

$$\Delta H^0 = 247\ kJ/mol$$

$$\Delta G^0 = 170\ kJ/mol$$

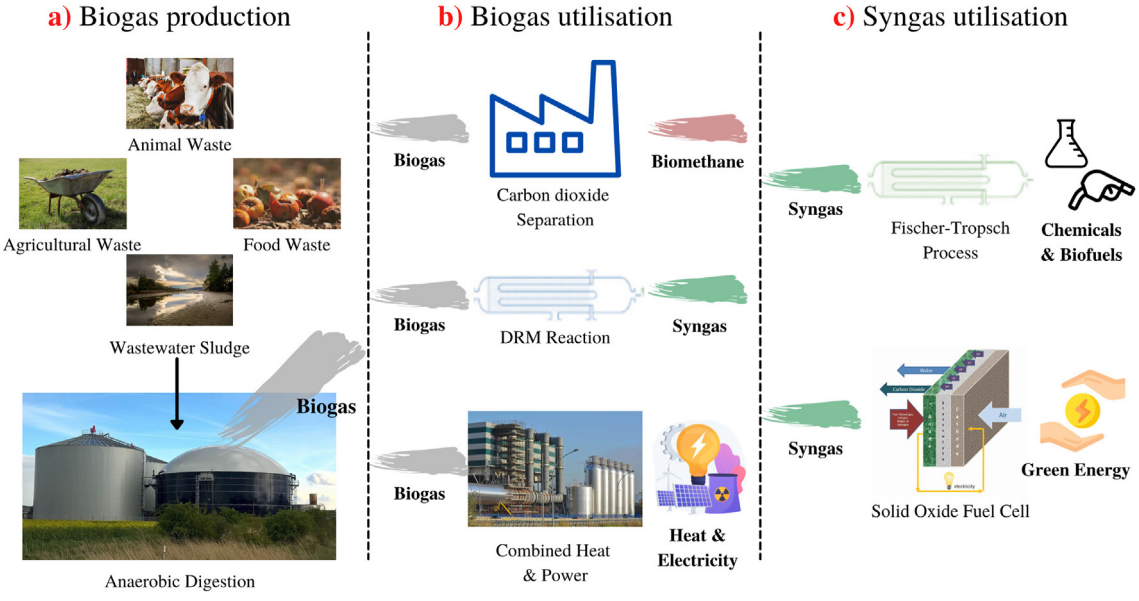

Fig. 1 – Biogas life cycle: a) Biogas production; b) Biogas utilisation; c) Syngas utilisation.

Even though the ORM (Eq. (1)) is presumably the most attractive option given its autothermic nature which results in significant energy savings, safety concerns associated with oxygen use limit its interest to industrial and large-scale applications [12]. The most popular technologies are the BRM (Eq. (2)) and the DRM (Eq. (3)). The first one leads to a syngas H_2/CO mixture ratio of a maximum of 2, meanwhile the last one can achieve a molar ratio of 1 [13]. However, in the context of a circular economy when a CO_2 utilisation route is pursued, CO_2 conversion may prevail over H_2/CO ratio as selection criteria for the optimal route. Herein, DRM takes the edge over BRM as reported elsewhere [14].

In any case, the conditions used for reforming also favour other side reactions (Eqs. (4)–(7)), in which carbon deposits (C*) are formed as follows [15]:

$$Methane\ decomposition: CH_4 \rightleftharpoons C^* + 2\,H_2 \quad \text{(Eq.4)}$$

$$\Delta H^0 = 75\ kJ/mol$$

$$Boudouard\ reaction: 2\,CO \rightleftharpoons C^* + CO_2 \quad \text{(Eq.5)}$$

$$\Delta H^0 = -172\ kJ/mol$$

$$CO_2\ hydrogenation: CO_2 + 2\,H_2 \rightleftharpoons C^* + 2\,H_2O \quad \text{(Eq.6)}$$

$$\Delta H^0 = -90\ kJ/mol$$

$$CO\ hydrogenation: CO + H_2 \rightleftharpoons C^* + H_2O \quad \text{(Eq.7)}$$

$$\Delta H^0 = -131\ kJ/mol$$

The formation of carbon deposits leads to catalysts deactivation, so it is important to find materials capable of minimizing carbon formation.

Besides these reactions that can deactivate the catalyst, there is also a side reaction that would decrease the H_2 yield, the Reverse Water Gas Shift (RWGS):

$$RWGS\ reaction: CO_2 + H_2 \rightleftharpoons CO + H_2O \quad \text{(Eq.8)}$$

$$\Delta H^0 = 46\ kJ/mol$$

When it comes to catalysts selection, Ni-based catalysts have shown a good activity and conversion of biogas into syngas [16–18], but they are textbook example for coking and sintering [19,20]. It has also been reported that noble metal-based catalysts have a greater activity and conversion, but in addition, they have more stability and higher coking resistance yet are expensive and less available [21]. For these very reasons bimetallic alloys comprised of Ni and low amounts of noble metals (*i.e.* Pd, Rh, Pt, Ru) are interesting in reforming processes.

Irrespectively of the selected formulation, it is clear that catalysts stability (resistance to the different deactivation phenomena) is crucial for an optimal process design. Frequently in heterogeneous catalysis, deactivation issues are resolved by catalyst regeneration. For instance, thermal treatments to remove carbon deposits or get rid of potential sulfides [22].

The sequence of activity for the DRM using M/MgO (M≡Ir,Ni,Pd,Pt,Rh,Ru) catalysts is Ru > Rh > Ni » Ir,Pt,Pd considering the presence of sulfur compounds [23]. Comparing Ru and Rh, the regeneration of Ru catalysts is much lower than that of Rh, so it seems that the best option for our objective is a bimetallic Ni–Rh catalyst [24].

Beyond the active phase, the support choice is also essential to ensure an adequate performance. For reforming reactions given the demanding process conditions (high temperatures) thermal and mechanical stability are key factors to consider. In this regard, alumina supports (Al_2O_3) offers an excellent balance thermal/mechanical property while also displaying high specific area which enhances metallic dispersion. However, the acidic sites of this kind of supports can increase coke formation. That is why ceria (CeO_2) is an interesting redox promoter. Indeed, ceria allows a flexible tunning of the acid/base properties of the support and provides excellent oxygen mobility, preventing carbon deposition via oxidation of the coke precursors [13].

Several authors have studied bimetallic Ni–Rh catalysts for the DRM reaction [25,26], yet the specific role of Rh and how it benefits catalytic performance is not fully addressed. Particularly, short-term stability test and insufficient of post-reaction analysis in the current reports pose some questions regarding the fundamental role of Rh in the bimetallic formulation. So, under these premises, this work focuses on the development of an advanced multicomponent catalysts Ni–Rh/CeO_2–Al_2O_3 whose performance is compared to a bare monometallic Ni/CeO_2–Al2O_3 system. Catalytic activity and stability results as well as pre- and post-reaction characterisation will be discussed to understand the beneficial effect of noble metal addition.

Experimental

Catalysts preparation

The support used was a commercial ceria-alumina oxidic support with 20 wt% of CeO_2 (*Puralox, SASOL*).

The monometallic catalyst was prepared by wet impregnation, where the support was first impregnated with $Ni(NO_3)_2{\cdot}6H_2O$ (Sigma-Aldrich) diluted in distilled water, evaporated at reduced pressure in a rotavapor, dried overnight at 100 °C and calcined at 550 °C for 4 h.

In a similar procedure, the bimetallic catalyst was prepared by wet co-impregnation, where the support was impregnated with $Ni(NO_3)_2{\cdot}6H_2O$ (Sigma-Aldrich) and $RhCl_3$ (Sigma-Aldrich) diluted in distilled water, evaporated at reduced pressure in a rotavapor, dried overnight at 100 °C and calcined at 550 °C for 4 h.

In all cases the NiO content is calculated to be 10 wt% and 0.5 wt% Rh for the bimetallic sample. These ratios were chosen based on previous works [27–29].

Characterisation techniques

The textural properties of the samples were evaluated from nitrogen adsorption-desorption isotherms at liquid nitrogen temperature in a Micromeritics Tristar II apparatus. Before

analysis, the samples were degassed at 150 °C for 8 h in vacuum.

On one hand, the specific surface area (S_{BET}) was determined by the Brunauer-Emmet-Teller (BET) method [30] and corresponds to the sum of the inner surface of the pore plus the outer surface of the grains. Additionally, the Barrett-Joyner-Halenda (BJH) method was used for determining the pore size distribution using the desorption isotherm. Pore volume represents the inner and outer granular volume, and the average pore size was calculated as the ratio of the pore volume and the specific surface area and normalized using a coefficient that depends on the pores shape [31].

Scanning electron microscopy (SEM) analysis was performed on the calcined samples in a vacuum, using a JEOL 5400 microscope equipped with an EDS analyser (Oxford Link).

X-ray diffraction measurements were carried out in a X'Pert Pro PANalytic instrument. The diffraction patterns were recorded at 40 mA and 45 kV using Cu-Kα radiation (λ = 0.154 nm). The 2θ angle was increased using a step size of 0.05° and a step time of 300 s in a range of 10 to 90°.

Temperature programmed reduction (TPR) measurements were conducted in a conventional U-shaped quartz reactor connected with a thermal conductivity detector (TCD), passing a flow of 50 mL/min of 5% H_2 diluted in Ar. TPR experiments were performed using approximately 50 mg of each catalyst at a heating rate of 10 °C/min from room temperature (RT = 25 °C) to 900 °C. A mixture containing acetone and dry ice was used as a cold trap to remove the water formed throughout the procedure.

Temperature programmed oxidation (TPO) experiments were carried out after the long-term stability tests to investigate the carbon species deposited on the catalyst surface. TPO analysis were conducted in a U-shaped quartz reactor coupled to a PFEIFFER Vacuum PrismaPlus mass spectrometer. 25 mg of both samples were heated up to 900 °C at a rate of 10 °C/min in a calibrated flow of 50 mL/min (5% O_2, 95% He).

Catalytic activity and stability

Catalytic performance was evaluated in a fixed-bed continuous-flow reactor described elsewhere [32] in which 100 mg of undiluted catalyst were loaded for each run. Prior to the reaction, the samples were *in situ* reduced in a flow of 10% H_2/N_2 at 850 °C for 1 h. The reaction was performed at atmospheric pressure passing a flow of 100 mL/min of $CO_2/CH_4/N_2$ (molar ratio of 1:1:6) and decreasing successively the temperature from 850 °C down to 550 °C until achieving the steady state each 50 °C. The WHSV (Weight Hourly Space Velocity) was fixed at 60 $L/g_{cat}\cdot h$. All the gases involved in the experiments were monitored by utilising an on-line gas analyser (ABB-AO2020) which was equipped with both IR and TCD detectors.

The catalytic stability of both mono and bimetallic materials was also studied. For this purpose, 100 mg of each catalyst were reduced under the same conditions as for the catalytic activity tests, and then the reaction conditions were evaluated at atmospheric pressure passing the same flow conditions as above at 650 °C for 48 h. A second stability study was carried out at 850 °C for 48 h.

The catalytic results obtained have been expressed in terms of conversions of both reactant gases and the H_2/CO molar ratio. The equations used to estimate these parameters are as follows:

$$CH_4\ conversion\ (\%) = \frac{n_{CH_4 in} - n_{CH_4 out}}{n_{CH_4 in}} \cdot 100 \quad \text{(Eq.9)}$$

$$CO_2\ conversion\ (\%) = \frac{n_{CO_2 in} - n_{CO_2 out}}{n_{CO_2 in}} \cdot 100 \quad \text{(Eq.10)}$$

$$H_2/CO = \frac{n_{H_2}}{n_{CO}} \cdot 100 \quad \text{(Eq.11)}$$

Being *n* the molar flow of CH_4, CO_2, H_2, and CO respectively and the subscripts *in* or *out* correspond to the inlet or the outlet reactor flow.

Results and discussion

Characterisation of solid catalysts

The textural properties (S_{BET}, and pore size and volume) of the catalysts and the commercial support are summarized in Table 1. As can be observed, the specific surface areas of the catalysts are quite similar. This indicates a good dispersion of the metals on the surface of the support, which will have a positive effect on the activity of the materials. Likewise, both pore volume (V_{pore}) and pore width (D_{pore}) are almost identically, showing that no agglomeration of metal particles has occurred on the catalyst and that the pores support have not been blocked.

Besides that, the textural properties obtained for the ceria-promoted alumina support suggest that both Ni and Rh are introduced into the pores of the support, so that the specific surface area, pore volume and pore width decrease.

In addition, the nitrogen adsorption/desorption isotherms at 77 K have been obtained for both catalysts as shown in Figure S1. According to IUPAC classification [33], four isotherm types are usually found in catalyst characterisation, and each isotherm shape depends directly on the solid porous texture. In our case, both isotherms correspond to a *type IV* isotherm, which is related to a mesoporous material (pore size between 2 nm and 50 nm). Besides, there is also a classification of the type of hysteresis, being the *type H1* found in our isotherms. This kind of hysteresis is characteristic of solids consisting of particles traversed by quasi-cylindrical channels or consisting of aggregates (consolidated) or agglomerates (unconsolidated) of spheroidal particles, and the pores may be uniform in size and shape.

Figure S2 shows the pore size distribution obtained by BJH method for both catalytic materials. As can be noted, both pore distribution curves are very similar confirming that there

Table 1 – Textural properties of the support and prepared catalysts.

Sample	S_{BET} (m^2/g)	V_{pore} (cm^3/g)	D_{pore} (Å)
$CeO_2–Al_2O_3$	159	0.39	71.9
$Ni/CeO_2–Al_2O_3$	132	0.31	67.7
$Ni–Rh/CeO_2–Al_2O_3$	138	0.32	66.6

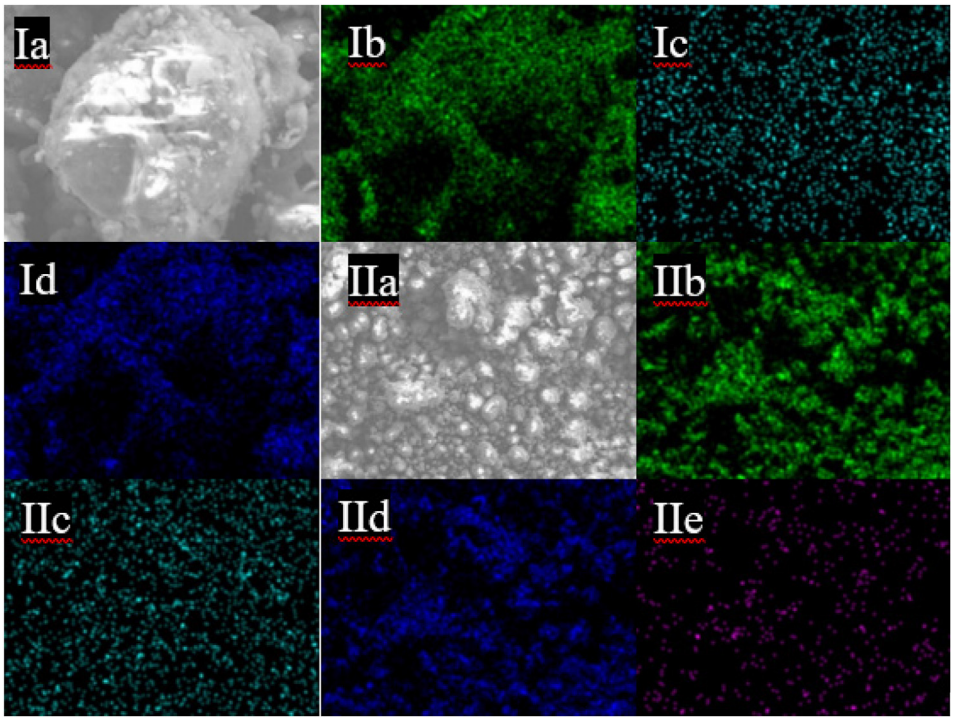

Fig. 2 – SEM micrographs of both calcined catalysts: (I)Ni/CeO_2–Al_2O_3; (II)Ni–Rh/CeO_2–Al_2O_3; where (a) general view; (b) Ce mapping; (c) Ni mapping; (d) Al mapping; (e) Rh mapping.

are not agglomeration of metal particles and the material cavities have not been blocked.

The morphology of the calcined catalysts is shown in the SEM micrographs provided in Fig. 2. Analysing the distribution of elements in the different mappings, we can confirm that both Ni and Rh are well dispersed and homogeneously distributed on the surface of the catalysts, corroborating a successful synthesis for both samples.

The structure of both prepared catalysts was analysed by means of X-Ray Diffraction (XRD). Both samples were firstly analysed after calcination at 550 °C (Fig. 3a). From this figure, it can be observed that all samples contain the typical diffraction lines corresponding to the (111), (200), (220) and (311) crystalline planes expected for the CeO_2 fluorite-like phase while the peaks corresponding to the (311) and (440) crystalline planes are ascribed to the γ-Al_2O_3 phase [34].

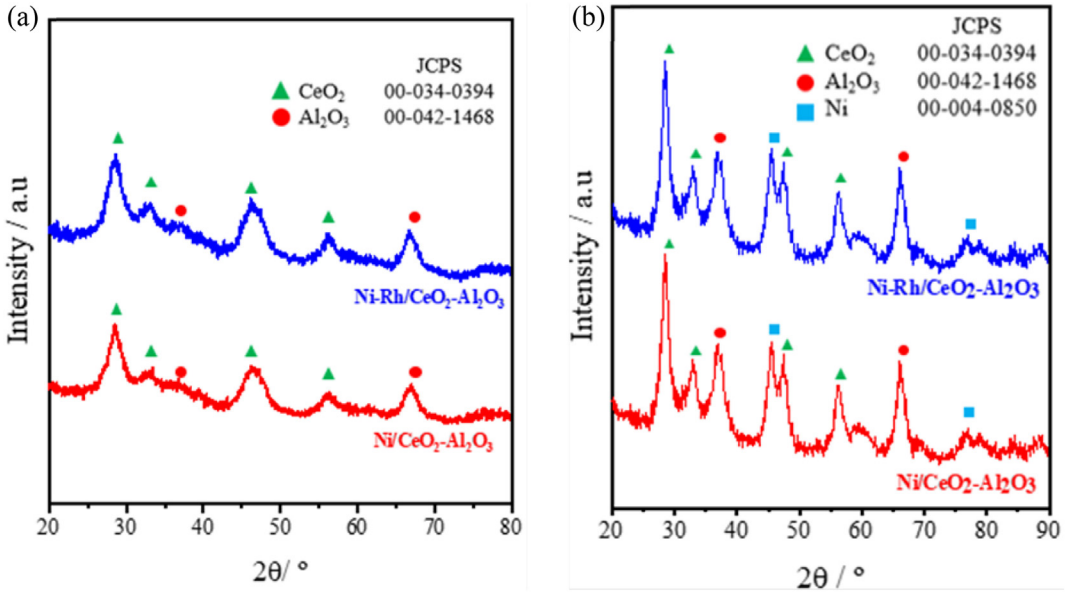

Fig. 3 – XRD of: a) calcined samples (550 °C); b) reduced samples (850 °C).

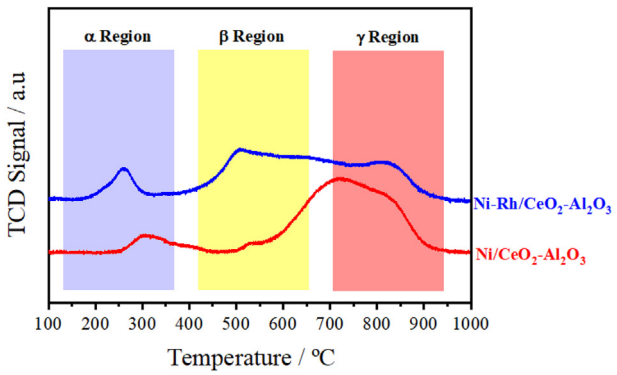

Fig. 4 – H_2-TPR profiles of both samples.

Fig. 3b shows the XRD patterns for the samples after reduction in a flow of 10% H_2/N_2 at 850 °C for 1 h. Hence, the diffraction lines related to metallic Ni can be clearly seen, although the metallic Rh peaks were hardly observed due to the high dispersion and/or low loading of the noble metal.

An overall idea of the redox behaviour and the metal-support interactions was gathered by Temperature Programmed Reduction (TPR) analysis. The TPR profiles obtained for both catalysts are presented in Fig. 4. Notably three different regions are distinguished. First, *α Region* (150–350 °C) shows the reduction of surface ceria [35–37], which is enhanced on the bimetallic catalyst due to the spill-over phenomenon [38]. The *β Region* (450–650 °C) exhibits the reduction of NiO with low to medium strength of interaction with the support. Finally, the reduction of NiO with high strength of interaction with the support occurs at temperatures above 700 °C (*γ Region*) [39].

Comparing both reduction profiles, we can see that the addition of rhodium improves notably the reducibility of Ni, facilitating its reduction at lower temperatures. This higher reducibility implies better redox properties, and these redox characteristics may enhance the catalytic performance during the DRM reaction.

DRM catalytic activity

The reduced catalysts were tested in the DRM reaction at a temperature range of 550–850 °C and at atmospheric pressure with a CO_2/CH_4 molar ratio 1:1. As we can see in Fig. 5.a, CH_4 conversions were lower than CO_2 conversions, which may suggest that the CH_4 activation is more difficult and requires higher temperatures in good agreement with DFT results [40]. The activation and cleavage of C–H bonds is more energetic than CO_2 dissociation.

On the other hand, comparing the results between both catalysts, no significant differences are observed in the carbon dioxide and methane conversions, with similar conversion levels for the monometallic catalyst and the bimetallic one.

In terms of the H_2/CO molar ratio (Fig. 5b), both catalysts also showed similar results. However, this molar ratio stays over 1 throughout the reactions, so we can conclude that H_2 concentration is higher than CO concentration. This is an interesting for biogas reforming via DRM since typical H_2/CO are slightly lower (typically close to 1). The main reason of this observation is the presence of multiple parallel reactions described above in the introduction section either consuming CO or producing H_2, *i.e.* the RWGS/WGS process which is effectively catalysed by Ni–CeO_2 systems [41].

Fig. 6 shows the XRD of the spent catalysts. Apart from the diffraction peaks of the metallic and support phases, we can observe a higher intensity in the 20-40° 2θ zone for the monometallic catalyst than for the bimetallic one. This testifies the formation of carbon deposits as will be well discussed further below.

DRM catalytic stability

Stability tests show how efficient catalysts are over long reaction runs and commonly stability is more important than activity in commercial catalysts design since it determines the frequency of start-up/shutdowns operations and the catalysts regeneration cost.

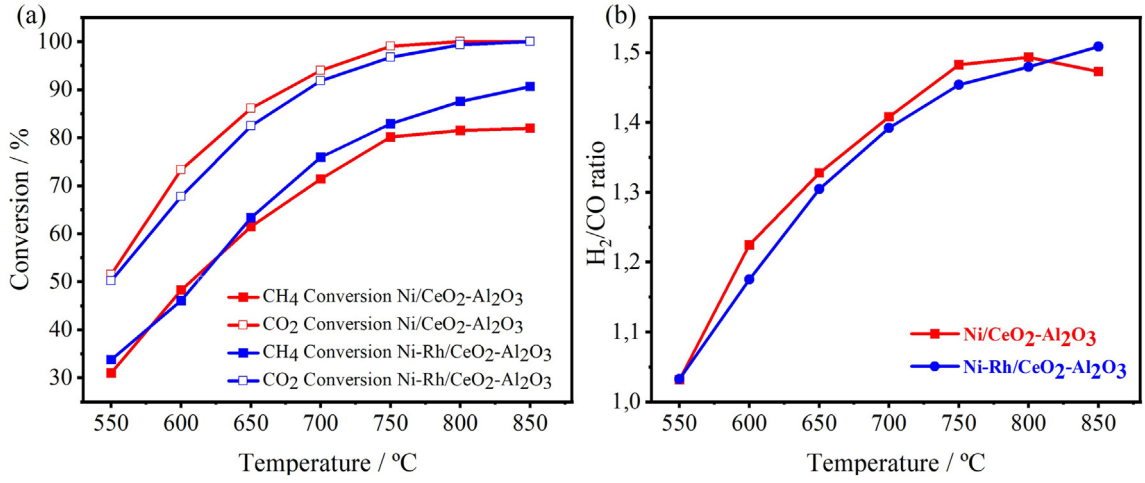

Fig. 5 – DRM catalytic activity: a) CO_2 & CH_4 conversions; b) H_2/CO molar ratio.

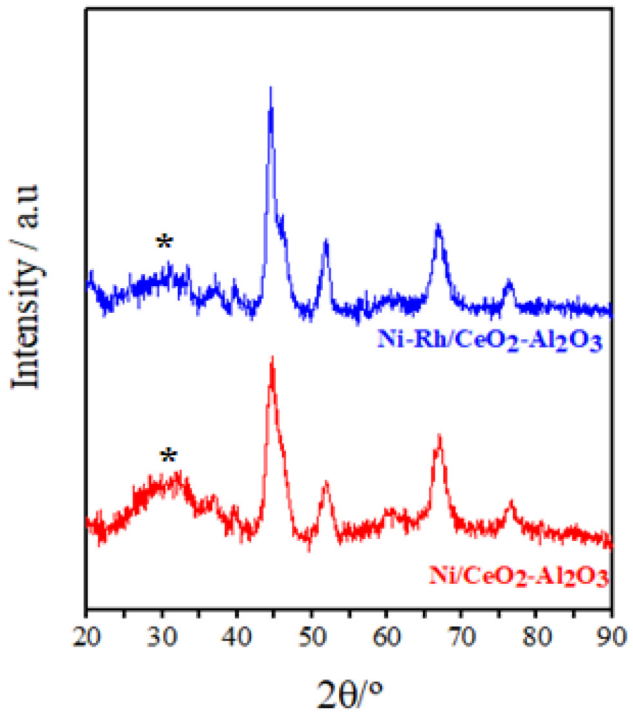

Fig. 6 – XRD of spent samples.

Hence, we have performed stability studies at two different temperatures. This way, we will be able to study the carbon deposition tolerance and metal sintering resistance of both catalysts in more in-depth manner. On the hand we will assess the coking tolerance at two different operation regimes and on the other hand we will evaluate the sintering resistance when increasing the thermal stress on the catalyst's particles.

The first stability test was performed at 650 °C. As shown in Fig. 7, both methane and carbon dioxide conversions for the $Ni/CeO_2–Al_2O_3$ sample decrease with time-on-stream, while conversions for the $Ni–Rh/CeO_2–Al_2O_3$ sample remain practically constant over the 48 h of the test. This result clearly evidences the superiority of the bimetallic formulation showcasing the positive impact of small amounts of Rh.

In order to study the carbonaceous deposits over both catalysts, TPO and XRD analyses were performed on the spent samples after the stability test.

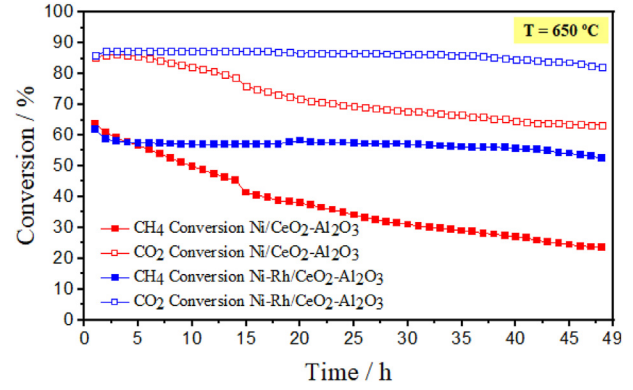

Fig. 7 – 650 °C-Stability test results.

The peaks observed in the TPO diagram (Fig. 8a) represent the generation of CO_2 by the oxidation of the carbon deposits formed, so it can be affirmed that the carbon deposited in the Ni–Rh catalyst is minimal compared to that of the reference sample. The temperature at which the CO_2 maximums appear provides information on the nature of the carbonaceous species deposited on the catalyst surface. Generally speaking, carbonaceous deposits have different structure orders and morphologies, and, in our case, we can distinguish between three types [42–50]:

The first peak appears at 300–400 °C and corresponds to a very labile amorphous carbon (C_α) which can be removed at low temperatures. The second peak appears at ~500 °C and corresponds to graphitic carbon (C_β) which is very thermally stable. The C_β is hardly removed by gasification so it leads to severe catalytic deactivation. Finally, the C_γ species were ascribed to carbon nanotubes, they appear at ~650 °C.

As we can see in Fig. 8.a, post-stability (650 °C) TPO analysis show more C_β deposits on the monometallic catalyst than on the bimetallic one. This justifies the continuous decrease of CH_4 and CO_2 conversions for the $Ni/CeO_2–Al_2O_3$ which is related to carbon poisoning and evidences the poorer performance of the reference material compared to the advanced bimetallic formulation. In addition, the XRD analyses of both spent samples (Fig. 8b) also show a clear difference since there is a peak at 26° approximately in the monometallic sample that it is not seen in the bimetallic sample. This peak corresponds to graphitic carbon deposits because it has a crystalline structure determined [51], thus confirming that there are more graphitic carbon deposits on the monometallic catalyst in fair agreement with the TPO analyses.

The second stability test was performed at 850 °C (Fig. 9). In this instance, the CO_2 conversions decrease as the same way for both catalysts, going from almost 100%–95% at the end of the experiment. Nonetheless, the methane conversion for the $Ni/CeO_2–Al_2O_3$ sample decreases from 97% down to 75% while the CH_4 conversion for the $Ni–Rh/CeO_2–Al_2O_3$ sample declines less, going from almost 95%–80%. Even so, these conversions are higher than those achieved during the stability test at 650 °C given the endothermic nature of the reaction.

As in the previous case, the TPO analyses of the post-stability samples at 850 °C also represent three very distinct peaks corresponding to the three types of carbon deposits mentioned above (Fig. 10a). In this case, the area under the curve of $Ni–Rh/CeO_2–Al_2O_3$ sample is significantly lower than the area under the curve of $Ni/CeO_2–Al_2O_3$ sample, which reconfirms that the addition of Rh to the Ni catalyst improves coking resistance. In fact, with a view to facilitate its visualisation, the signal of the former has been multiplied by a factor of 4, as it was difficult to separate the two peaks on a normal scale. It must be emphasised the carbon deposition is thermodynamically more favoured at lower temperatures between 600 and 750 °C. In any case our bimetallic sample outperformed the reference catalysts in both temperature regimes.

However, graphitic carbon formation was lower on the monometallic catalyst in this test, as coke formation is more favoured at lower temperatures. A particularity of this stability test is that it is possible to observe how the sintering phenomenon affects the monometallic catalyst with the XRD

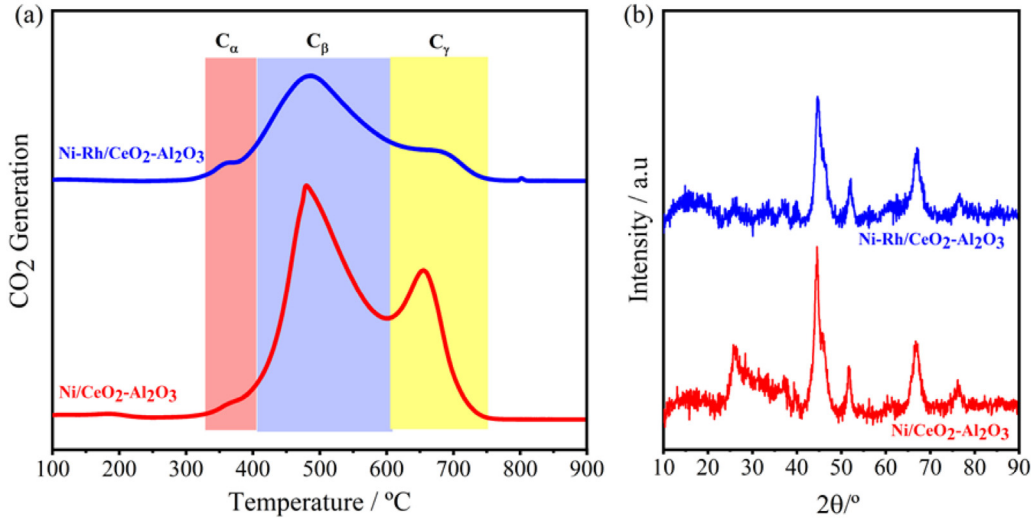

Fig. 8 – Post characterisation after stability test at 650 °C: a) TPO; b) XRD.

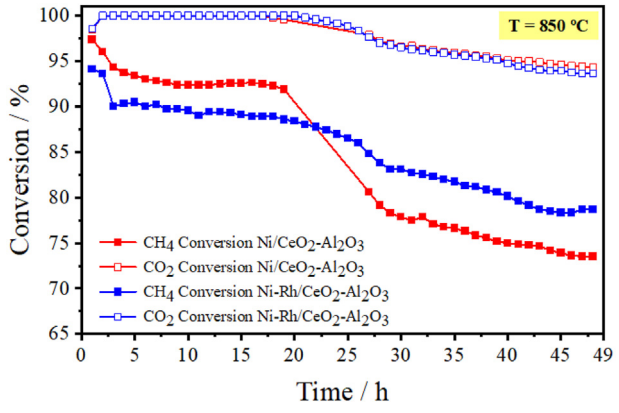

Fig. 9 – 850 ºC-Stability test results.

of these samples (Fig. 10b). The peak of Ni located at 51.8° was used to estimate the crystallite size by means of Scherrer equation. It was found that the crystallite size is higher in the monometallic catalyst. To make a comparison with the Ni crystallite size before reaction, the same procedure was performed with the deconvoluted Ni peak of both reduced catalysts. In the case of the monometallic sample, the Ni crystallite size increased from 12 nm to 17.5 nm, while in the bimetallic catalyst this value increased from 11.7 nm to 13 nm. This is evidence of how the addition of a bimetallic active phase prevents the sintering deactivation of the catalysts since the segregation of Ni species from stable bimetallic formulations is somewhat less energetically favourable in comparison to pure Ni particles [52,53].

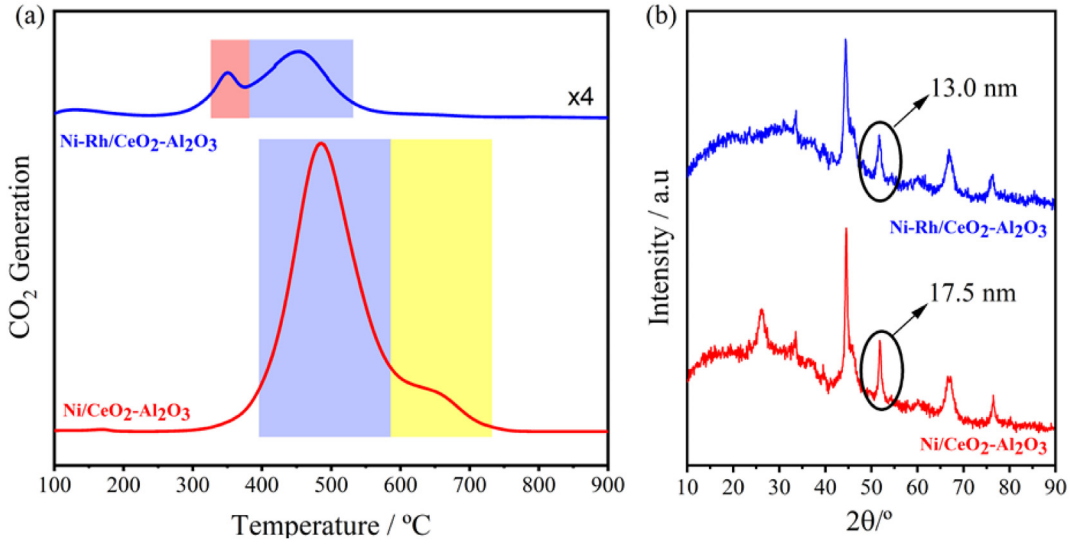

Fig. 10 – Post characterisation after stability test at 850 °C: a) TPO; b) XRD.

Comparing the results obtained in the stability tests at 650 °C and 850 °C, we can state that the deactivation at 650 °C is mainly caused by the formation of coke, while at 850 °C the deactivation by sintering prevails, as less carbon formation is observed. In both situations, the bimetallic catalyst stands out as a promising alternative.

At 650 °C the predominant secondary reaction is methane decomposition (Eq. (4)) where carbon deposits and hydrogen are formed from methane. This explains the low methane yields and that the H_2/CO ratio remains above 1 at this temperature. At 850 °C, however, the reverse reaction of the Boudouard reaction (Eq. (5)) starts to occur, where the carbon formed with CO_2 is converted to CO. This could decrease the H_2/CO ratio, but C_β is very thermally stable, and the CO formation is not large enough to counteract the excessive H_2 formation.

Conclusions

Biogas conversion to H_2-rich syngas represents a straightforward approach for greenhouses valorisation in the context of a circular economy. Herein, a multicomponent catalyst based on Ni–Rh bimetallic active phase supported on a ceria-promoted alumina (Ni–Rh/CeO_2–Al_2O_3) has been prepared and tested in biogas upgrading via DRM. The performance of this advanced system has been compared to that of a reference monometallic nickel homologue (Ni/CeO_2–Al_2O_3). Different pre-reaction and post-reaction characterisation tests have been carried out, as well as a reaction monitoring based on the CH_4 and CO_2 conversions and the H_2/CO molar ratio obtained. The starting hypothesis suggested better performances for the bimetallic catalyst than for the monometallic one.

TPR experiments showed a higher reducibility for the bimetallic sample compared to the monometallic one, which implies better redox properties, enhancing the catalytic performance during the DRM reaction.

In the catalytic activity test, the differences observed are negligible however key discrepancies are observed in the catalysts' stability. The results obtained in the different stability tests show that there is indeed a synergic Ni–Rh effect that improves catalytic stability, thus the conversions on the bimetallic catalyst remain almost constant over long-term runs while the monometallic catalyst suffers a significant activity drop showcasing its deactivation.

Post-stability TPO experiments showed the formation of two different carbonaceous species, an amorphous carbon and a crystalline carbon, the latter being the cause of deactivation as it is very thermally stable. Our results demonstrate that the monometallic systems nucleate greater concentration of carbon than the advanced bimetallic sample being carbon deposition favoured in the low-temperature range (*i.e.* 650 °C).

With the stability test at 850 °C the sintering of nickel particles can be also observed, with a remarkable increase on the Ni clusters size on the monometallic catalyst compared to the bimetallic which demonstrates a greater tolerance towards active phase agglomeration.

Overall, this paper showcases the key role played by heterogeneous catalysis within CO_2 conversion technologies and the research still needed to keep refining catalytic formulations to avoid deactivation seeking for an optimal operation. In particular, this work has demonstrated that the addition of low amounts of Rh significantly improves the catalytic performance, reducing coke formation and sintering. A novel angle of this work is the proven coking resistance of our multicomponent catalysts in the low-temperature DRM window. This is a remarkable result beyond the catalysts optimization opening a new research avenue for the design of low-temperature DRM units resulting in a potential tangible reduction in energy consumption and overall process operation costs.

In any case, the design of advanced multicomponent catalysts as the one presented herein will contribute to facilitate the transition towards greener industrial processes to produce low-carbon fuels and added value chemicals.

Declaration of competing interest

The authors declare that they have no known competing financial interests or personal relationships that could have appeared to influence the work reported in this paper.

Acknowledgements

Financial support for this work was gather from Spanish Ministry of Science and Spanish Ministry of Science and Innovation through the projects PLEC2021-008086, RYC2018-024387-I as well as the project PID2019-108502RJ-I00. This work was also partially funded by the University of Seville via the VI PPIT grant scheme for talented researchers. Sergio Carrasco would also like to acknowledge the Sociedad Española de Catálisis (SECAT) for his fellowship. Funding from the European Commission through the BIOALL project (Grant Agreement: 101008058) SASOL is kindly acknowledged for providing the catalysts' supports.

Appendix A. Supplementary data

Supplementary data to this article can be found online at https://doi.org/10.1016/j.ijhydene.2023.03.301.

REFERENCES

[1] Yoro KO, Daramola MO. CO2 emission sources, greenhouse gases, and the global warming effect. In: Advances in carbon capture. Elsevier; 2020. p. 3–28. https://doi.org/10.1016/b978-0-12-819657-1.00001-3.

[2] Kappelle M. United in science 2020 - UN climate report. 2020. https://doi.org/10.13140/RG.2.2.12801.28004.

[3] Boucher O, Friedlingstein P, Collins B, Shine KP. The indirect global warming potential and global temperature change potential due to methane oxidation. Environ Res Lett 2009;4. https://doi.org/10.1088/1748-9326/4/4/044007.

[4] Ullah Khan I, Hafiz Dzarfan Othman M, Hashim H, Matsuura T, Ismail AF, Rezaei-DashtArzhandi M, Wan

Azelee I. Biogas as a renewable energy fuel – a review of biogas upgrading, utilisation and storage. Energy Convers Manag 2017;150:277–94. https://doi.org/10.1016/j.enconman.2017.08.035.
[5] Goumenou D, Arellano-Garcia Tomas Ramirez Reina H. Upgrading biogas to syngas via dry reforming. 2016.
[6] Ryckebosch E, Drouillon M, Vervaeren H. Techniques for transformation of biogas to biomethane. Biomass Bioenergy 2011;35:1633–45. https://doi.org/10.1016/j.biombioe.2011.02.033.
[7] Mota N, Alvarez-Galvan C, Navarro RM, Fierro J. Biogas as a source of renewable syngas production: advances and challenges. 2011. https://doi.org/10.4155/bfs.11.15.
[8] Baena-Moreno FM, Sebastia-Saez D, Wang Q, Reina TR. Is the production of biofuels and bio-chemicals always profitable? Co-production of biomethane and urea from biogas as case study. Energy Convers Manag 2020;220:113058. https://doi.org/10.1016/J.ENCONMAN.2020.113058.
[9] Budzianowski WM, Postawa K. Renewable energy from biogas with reduced carbon dioxide footprint: implications of applying different plant configurations and operating pressures. Renew Sustain Energy Rev 2017;68:852–68. https://doi.org/10.1016/j.rser.2016.05.076.
[10] dos Santos RG, Alencar AC. Biomass-derived syngas production via gasification process and its catalytic conversion into fuels by Fischer Tropsch synthesis: a review. Int J Hydrogen Energy 2020;45:18114–32. https://doi.org/10.1016/j.ijhydene.2019.07.133.
[11] Kumar N, Shojaee M, Spivey JJ. Catalytic bi-reforming of methane: from greenhouse gases to syngas. Curr Opin Chem Eng 2015;9:8–15. https://doi.org/10.1016/j.coche.2015.07.003.
[12] Stroud T, Smith TJ, le Saché E, Santos JL, Centeno MA, Arellano-Garcia H, Odriozola JA, Reina TR. Chemical CO2 recycling via dry and bi reforming of methane using Ni-Sn/Al2O3 and Ni-Sn/CeO2-Al2O3 catalysts. Appl Catal, B 2018;224:125–35. https://doi.org/10.1016/j.apcatb.2017.10.047.
[13] le Saché E, Johnson S, Pastor-Pérez L, Horri BA, Reina TR. Biogas upgrading via dry reforming over a Ni-Sn/CeO2-Al2O3 catalyst: influence of the biogas source. Energies 2019;12. https://doi.org/10.3390/en12061007.
[14] le Saché E, Pastor-Pérez L, Garcilaso V, Watson DJ, Centeno MA, Odriozola JA, Reina TR. Flexible syngas production using a La2Zr2-xNixO7-δ pyrochlore-double perovskite catalyst: towards a direct route for gas phase CO2 recycling. Catal Today 2020;357:583–9. https://doi.org/10.1016/j.cattod.2019.05.039.
[15] Azancot L, Bobadilla LF, Centeno MA, Odriozola JA. IR spectroscopic insights into the coking-resistance effect of potassium on nickel-based catalyst during dry reforming of methane. Appl Catal, B 2021;285. https://doi.org/10.1016/j.apcatb.2020.119822.
[16] le Saché E, Pastor-Pérez L, Watson D, Sepúlveda-Escribano A, Reina TR. Ni stabilised on inorganic complex structures: superior catalysts for chemical CO2 recycling via dry reforming of methane. Appl Catal, B 2018;236:458–65. https://doi.org/10.1016/j.apcatb.2018.05.051.
[17] Price CAH, Arnold W, Pastor-Pérez L, Amini-Horri B, Reina TR. Catalytic upgrading of a biogas model mixture via low temperature DRM using multicomponent catalysts. Top Catal 2020;63:281–93. https://doi.org/10.1007/s11244-019-01216-8.
[18] Wang C, Zhang Y, Wang Y, Zhao Y. Comparative studies of non-noble metal modified mesoporous M-Ni-CaO-ZrO 2 (M = Fe, Co, Cu) catalysts for simulated biogas dry reforming. Chin J Chem 2017;35:113–20. https://doi.org/10.1002/cjoc.201600609.
[19] Bartholomew CH. Mechanisms of catalyst deactivation. Appl Catal A 2001:17–60. https://doi.org/10.1016/S0926-860X(00)00843-7.
[20] Kosari M, Askari S, Seayad AM, Xi S, Kawi S, Borgna A, Zeng HC. Strong coke-resistivity of spherical hollow Ni/SiO2 catalysts with shell-confined high-content Ni nanoparticles for methane dry reforming with CO2. Appl Catal, B 2022;310. https://doi.org/10.1016/J.APCATB.2022.121360.
[21] Bobadilla LF, Garcilaso V, Centeno MA, Odriozola JA. Monitoring the reaction mechanism in model biogas reforming by in situ transient and steady-state DRIFTS measurements. ChemSusChem 2017;10:1193–201. https://doi.org/10.1002/cssc.201601379.
[22] Boldrin P, Ruiz-Trejo E, Mermelstein J, Bermúdez Menéndez JM, Ramírez Reina T, Brandon NP. Strategies for carbon and sulfur tolerant solid oxide fuel cell materials, incorporating lessons from heterogeneous catalysis. Chem Rev 2016;116:13633–84. https://doi.org/10.1021/acs.chemrev.6b00284.
[23] Rostrup-Nielsen JR, Bak Hansen JH. CO2-reforming of methane over transition metals. J Catal 1993;144. https://doi.org/10.1006/jcat.1993.1312.
[24] Watanabe F, Kaburaki I, Shimoda N, Igarashi A, Satokawa S. Sulfur tolerance of noble metal catalysts for steam methane reforming. J Jpn Petrol Inst 2017;60. https://doi.org/10.1627/jpi.60.137.
[25] Hou Z, Yashima T. Small amounts of Rh-promoted Ni catalysts for methane reforming with CO2. Catal Lett 2003;89:193–7. https://doi.org/10.1023/A:1025746211314.
[26] Zhang Y, Wang G-C. Significant effect of Rh on the h-BN-supported Ni catalyst for dry reformation of CH4 : insights from density functional theory and microkinetic analysis. J Phys Chem C 2021;125:26530–41. https://doi.org/10.1021/acs.jpcc.1c08994.
[27] Yentekakis Iv, Panagiotopoulou P, Artemakis G. A review of recent efforts to promote dry reforming of methane (DRM) to syngas production via bimetallic catalyst formulations. Appl Catal, B 2021;296. https://doi.org/10.1016/J.APCATB.2021.120210.
[28] Yokota S, Okumura K, Niwa M. Support effect of metal oxide on Rh catalysts in the CH4-CO2 reforming reaction. Catal Lett 2002;84(1):131–4. https://doi.org/10.1023/A:1021097206196. 84 (2002).
[29] Tsipouriari VA, Efstathiou AM, Zhang ZL, Verykios XE. Reforming of methane with carbon dioxide to synthesis gas over supported Rh catalysts. Catal Today 1994;21:579–87. https://doi.org/10.1016/0920-5861(94)80182-7.
[30] Brunauer S, Emmett PH, Teller E. Adsorption of gases in multimolecular layers. J Am Chem Soc 1938;60(2):309–19. https://doi.org/10.1021/ja01269a023.
[31] García N, Ph M, Thesis D, Romero F, Antonio SJ, Gordón O. On the rate-limiting step of the WGS reaction: design of the model catalyst. 2017.
[32] le Saché E, Santos JL, Smith TJ, Centeno MA, Arellano-Garcia H, Odriozola JA, Reina TR. Multicomponent Ni-CeO2 nanocatalysts for syngas production from CO2/CH4 mixtures. J CO2 Util 2018;25:68–78. https://doi.org/10.1016/J.JCOU.2018.03.012.
[33] Leofanti G, Padovan M, Tozzola G, Venturelli B. Surface area and pore texture of catalysts. Catal Today 1998;41:207–19. https://doi.org/10.1016/S0920-5861(98)00050-9.
[34] Li Y, Wang X, Xie C, Song C. Influence of ceria and nickel addition to alumina-supported Rh catalyst for propane steam reforming at low temperatures. Appl Catal A 2009;357(2):213–22. https://doi.org/10.1016/j.apcata.2009.01.025.
[35] Schiaroli N, Lucarelli C, Iapalucci MC, Fornasari G, Crimaldi A, Vaccari A. Combined reforming of clean biogas over nanosized Ni–Rh bimetallic clusters. Catalysts 2020;10:1345. https://doi.org/10.3390/CATAL10111345.

[36] Trovarelli A, de Leitenburg C, Dolcetti G, Lorca JL. CO2 methanation under transient and steady-state conditions over Rh/CeO2 and CeO2-promoted Rh/SiO2: the role of surface and bulk ceria. J Catal 1995;151:111–24. https://doi.org/10.1006/JCAT.1995.1014.

[37] Özkara-Aydinoğlu Ş, Özensoy E, Aksoylu AE. The effect of impregnation strategy on methane dry reforming activity of Ce promoted Pt/ZrO2. Int J Hydrogen Energy 2009;34:9711–22. https://doi.org/10.1016/J.IJHYDENE.2009.09.005.

[38] Halabi MH, de Croon MHJM, van der Schaaf J, Cobden PD, Schouten JC. Low temperature catalytic methane steam reforming over ceria–zirconia supported rhodium. Appl Catal Gen 2010;389:68–79. https://doi.org/10.1016/J.APCATA.2010.09.004.

[39] López-Fonseca R, Jiménez-González C, de Rivas B, Gutiérrez-Ortiz JI. Partial oxidation of methane to syngas on bulk $NiAl_2O_4$ catalyst. Comparison with alumina supported nickel, platinum and rhodium catalysts. Appl Catal Gen 2012:437–8. https://doi.org/10.1016/J.APCATA.2012.06.014.

[40] Guharoy U, le Saché E, Cai Q, Reina TR, Gu S. Understanding the role of Ni-Sn interaction to design highly effective CO2 conversion catalysts for dry reforming of methane. J CO2 Util 2018;27:1–10. https://doi.org/10.1016/J.JCOU.2018.06.024.

[41] Pastor-Pérez L, Buitrago-Sierra R, Sepúlveda-Escribano A. CeO2-promoted Ni/activated carbon catalysts for the water–gas shift (WGS) reaction. Int J Hydrogen Energy 2014;39:17589–99. https://doi.org/10.1016/J.IJHYDENE.2014.08.089.

[42] Bai X, Xie G, Guo Y, Tian L, El-Hosainy HM, Awadallah AE, Ji S, jun Wang Z. A highly active Ni catalyst supported on Mg-substituted LaAlO3 for carbon dioxide reforming of methane. Catal Today 2021;368:78–85. https://doi.org/10.1016/J.CATTOD.2019.12.033.

[43] Guo Y, Li Y, Ning Y, Liu Q, Tian L, Zhang R, Fu Q, Wang Z-J. CO2 reforming of methane over a highly dispersed Ni/Mg–Al–O catalyst prepared by a facile and green method. Ind Eng Chem Res 2020;59:15506–14. https://doi.org/10.1021/acs.iecr.0c02444.

[44] Wen S, Liang M, Zou J, Wang S, Zhu X, Liu L, Wang Z-J. Synthesis of a SiO2 nanofibre confined Ni catalyst by electrospinning for the CO2 reforming of methane. J Mater Chem 2015;3:13299–307. https://doi.org/10.1039/c5ta01699a.

[45] Sun J, Wang S, Guo Y, Li M, Zou H, jun Wang Z. Carbon dioxide reforming of methane over nanostructured Ni/Al2O3 catalysts. Catal Commun 2018;104:53–6. https://doi.org/10.1016/J.CATCOM.2017.10.021.

[46] Guo Y, Zou J, Shi X, Rukundo P, Wang Z. A Ni/CeO2–CDC-SiC catalyst with improved coke resistance in CO2 reforming of methane. ACS Sustainable Chem Eng 2017;5:2330–8. https://doi.org/10.1021/acssuschemeng.6b02661.

[47] Zhang ZL, Verykios XE. Carbon dioxide reforming of methane to synthesis gas over supported Ni catalysts. Catal Today 1994;21:589–95. https://doi.org/10.1016/0920-5861(94)80183-5.

[48] Wang C, Jie X, Qiu Y, Zhao Y, Al-Megren HA, Alshihri S, Edwards PP, Xiao T. The importance of inner cavity space within Ni@SiO2 nanocapsule catalysts for excellent coking resistance in the high-space-velocity dry reforming of methane. Appl Catal, B 2019;259:118019. https://doi.org/10.1016/J.APCATB.2019.118019.

[49] Zhao Y, Wang C, Qiu Y, Zhang X, Zhang Y, Sun N, Zhao Y. Highlighting research from C Geometric design of a Ni@silica nano-capsule catalyst with superb methane dry reforming stability: enhanced confinement effect over the nickel site anchoring inside a capsule shell with an appropriate inner cavity †. Catal Sci Technol 2018;8:4877. https://doi.org/10.1039/c8cy01158c.

[50] Wang C, Sun N, Wei W, Zhao Y. Carbon intermediates during CO2 reforming of methane over Ni[sbnd]CaO[sbnd]ZrO2 catalysts: a temperature-programmed surface reaction study. Int J Hydrogen Energy 2016;41:19014–24. https://doi.org/10.1016/J.IJHYDENE.2016.08.128.

[51] Azancot L, Bobadilla LF, Santos JL, Córdoba JM, Centeno MA, Odriozola JA. Influence of the preparation method in the metal-support interaction and reducibility of Ni-Mg-Al based catalysts for methane steam reforming. Int J Hydrogen Energy 2019;44:19827–40. https://doi.org/10.1016/j.ijhydene.2019.05.167.

[52] Basu Bikramjit, Balani Kantesh. Advanced structural ceramics. Hoboken, N.J: Wiley; 2011.

[53] Morales-Cano F, Lundegaard LF, Tiruvalam RR, Falsig H, Skjøth-Rasmussen MS. Improving the sintering resistance of Ni/Al2O3 steam-reforming catalysts by promotion with noble metals. Appl Catal A 2015;498:117–25. https://doi.org/10.1016/J.APCATA.2015.03.016.